



Horizon 2020 Societal challenge 5:  
Climate action, environment, resource  
efficiency and raw materials

# VERIFY

## Observation-based system for monitoring and verification of greenhouse gases

GA number 776810, RIA

<b>Deliverable number (relative in WP)</b>	<b>D4.10</b>
<b>Deliverable name:</b>	Methane and nitrous oxide fluxes from the CIF
<b>WP / WP number:</b>	WP4
<b>Delivery due date:</b>	Month 42 (31/07/2021)
<b>Actual date of submission:</b>	Month 54 (06/07/2022)
<b>Dissemination level:</b>	Public
<b>Lead beneficiary:</b>	CEA-LSCE
<b>Responsible</b>	Isabelle Pison (CEA)
<b>Contributor(s):</b>	Rona Thompson, Espen Sollum, Massaer Kouyaté, Isabelle Pison, Antoine Berchet, Jean-Matthieu Haussaire
<b>Internal reviewer:</b>	Audrey Fortems-Cheiney, Grégoire Broquet

<b>Changes with respect to the DoA</b>
None
<b>Dissemination and uptake (Who will/could use this deliverable, within the project or outside the project?)</b>
<p>The results will be made available via the VERIFY project database and are currently available via a data server to the project partners.</p> <p>The results for methane fluxes are part of a paper being drafted for ESSD to describe the implementation of satellite data assimilation in the CIF and compare their impact on fluxes to the assimilation of surface data. They will also be used in a paper comparing the impact of atmospheric transport on inverse modelling results.</p>
<b>Short Summary of results (&lt;250 words)</b>
<p>This deliverable presents the CH<sub>4</sub> and N<sub>2</sub>O fluxes obtained by atmospheric inversion with the CIF interfaced with different atmospheric chemistry-transport models (FLEXPART, FLEXPART-EMPA, and CHIMERE). The fluxes were estimated over the European domain (15°W to 35°E and 33°N to 73°N) for the years 2006 to 2018 from all models.</p> <p>For CH<sub>4</sub>, the results from CHIMERE differed somewhat from the two FLEXPART models in where the posterior fluxes departed from the prior estimates, but were reasonably comparable in terms of the annual emissions at regional scales. For EU27 plus Norway, Switzerland and UK (EU27+3), the total mean emissions were 26, 22 and 24 Tg CH<sub>4</sub>/y, for CHIMERE, FLEXPART and FLEXPART-EMPA, respectively.</p> <p>For N<sub>2</sub>O, inversions were run with CHIMERE and FLEXPART (NILU). The results using the two models were very comparable at the level of EU27+3 with annual mean emissions for 2005-2018 of 0.98 and 1.07 TgN/y and with decreasing trends of 0.010 and 0.019 TgN/y per year for CHIMERE and FLEXPART, respectively.</p>
<b>Evidence of accomplishment (report, manuscript, web-link, other)</b>
<p>The retrieved fluxes will be accessible through VERIFY project database. Note that some of these data may be password protected during a consolidation phase and thus only accessible to the VERIFY partners (accessible through the internal share-point platform).</p>



due 31/07/2021

WP4\_Task4.10

VERIFY\_D4.10\_ Methane and nitrous oxide fluxes from the CIF\_v1

<b>Version</b>	<b>Date</b>	<b>Description</b>	<b>Author (Organisation)</b>
V0	16/02/2022	Creation/Writing	Isabelle Pison (LSCE)
V0.1	28/06/2022	Writing/Formatting/Delivery	Rona Thompson (NILU)
V1	06/07/2022	Formatting/Delivery on the Participant Portal	Aur�lie Paquirissamy (LSCE)

<b>1. Glossary</b>	<b>5</b>
<b>2. Executive Summary</b>	<b>6</b>
<b>3. Introduction</b>	<b>6</b>
<b>4. Methane and nitrous oxide fluxes from the CIF</b>	<b>9</b>
<b>4.1. Atmospheric transport models</b>	<b>9</b>
4.1.1. CHIMERE	9
4.1.2. FLEXPART	9
<b>4.2. Input data for inversions</b>	<b>10</b>
4.2.1. Atmospheric observations	10
4.2.2. Prior fluxes	10
4.2.3. Boundary conditions	12
<b>4.3. Inversion set-up</b>	<b>13</b>
4.3.1. Control vector	13
4.3.2. Uncertainties	13
<b>4.4. Results</b>	<b>15</b>
4.4.1. Methane mixing ratios	15
4.4.2. Methane fluxes	17
4.4.3. Nitrous oxide mixing ratios	20
4.4.4. Nitrous oxide fluxes	23
<b>5. Conclusions</b>	<b>26</b>
<b>6. References</b>	<b>27</b>

# 1. Glossary

Abbreviation / Acronym	Description/meaning
<b>CAMS</b>	Copernicus Atmosphere Monitoring System
<b>CHIMERE</b>	Chemistry-transport area-limited Eulerian model
<b>CIF</b>	Community Inversion Framework
<b>CTM</b>	Chemistry-Transport Model
<b>FLEXPART</b>	Flexible Particle Dispersion Model
<b>ECMWF</b>	European Centre for Medium-Range Weather Forecasts
<b>EDGAR</b>	The Emission Database for Global Atmospheric Research
<b>EU</b>	European Union
<b>GCP-CH4</b>	Global Carbon Project – Methane
<b>GFED</b>	Global Fire Emissions Database
<b>GHG</b>	Greenhouse gas
<b>GWP</b>	Global Warming Potential
<b>ICOS</b>	Integrated Carbon Observatory System
<b>IFS</b>	Integrated Forecasting System
<b>NOAA ESRL</b>	National Oceanic and Atmospheric Administration - Earth System Research Laboratories
<b>WDCGG</b>	World Data Center for Greenhouse Gases

## 2. Executive Summary

Atmospheric inverse modeling uses observations of atmospheric concentrations and atmospheric transport models to derive estimates of surface-atmosphere fluxes, such as of greenhouse gases (GHGs). Since they provide observation-based estimates of the fluxes, they are an important tool for verifying bottom-up model and inventory estimates. Inverse modeling has been used for about three decades for retrieving anthropogenic and/or natural GHG fluxes and over this time the atmospheric transport models have improved in terms of spatial resolution and physical parameterisations. In addition, the number of observations has expanded greatly, both with surface networks and satellite measurements. Surface measurements have low uncertainties, cover relatively long periods of time and sample the atmosphere in layers which are close to most emission sources (located at the surface or relatively close to the ground e.g. smoke stacks). The main uncertainties in fluxes from atmospheric inversions, come from the uncertainties in atmospheric transport, the limited coverage of the observations, and uncertain estimates for the prior and observational uncertainties.

Inter-comparisons between inversion frameworks and atmospheric transport models are important as a means to obtain estimates of the full, i.e., random and systematic, uncertainty for the fluxes from inversions. Several inter-comparison studies have been led in Europe to compare inversion derived fluxes over several years, such as (Bergamaschi et al., 2018). However, inter-comparisons have been limited by the fact that the inversion systems used are complex numerical systems with many input parameters, thus it is difficult to identify the causes of differences between them. Furthermore, since inversion frameworks are often only used by one group or institute, developments are the responsibility of only a small group of users, and improvements in methodology need to be implemented in each inversion framework separately. A step forward has been made in VERIFY with the development of the Community Inversion Framework (CIF), which is a Python-based set of inversion tools and can be interfaced with different atmospheric transport models (Berchet et al., 2021).

This report presents the results of methane ( $\text{CH}_4$ ) and nitrous oxide ( $\text{N}_2\text{O}$ ) inversions performed with the CIF interfaced with different atmospheric chemistry transport models, specifically, CHIMERE, and two versions of FLEXPART. The inversions all used the same prior fluxes (based on VERIFY results D4.3 and D4.6), surface atmospheric observations, and boundary conditions.

For  $\text{CH}_4$ , inversions were run with all 3 atmospheric transport models. The results from CHIMERE differed somewhat from the two FLEXPART models in where the posterior fluxes departed from the prior estimates, but were reasonably comparable in terms of the annual emissions at regional scales. For EU27 plus Norway, Switzerland and UK (EU27+3), the total mean emissions were 26, 22 and 24 Tg  $\text{CH}_4/\text{y}$ , for CHIMERE, FLEXPART and FLEXPART-EMPA, respectively.

For  $\text{N}_2\text{O}$ , inversions were run with CHIMERE and FLEXPART (NILU). The results using the two models were very comparable at the level of EU27+3 with annual mean emissions for 2005-2018



of 0.98 and 1.07 TgN/y and with decreasing trends of 0.010 and 0.019 TgN/y per year for CHIMERE and FLEXPART, respectively.

### 3. Introduction

Methane ( $\text{CH}_4$ ) and nitrous oxide ( $\text{N}_2\text{O}$ ) are the second and third most important GHGs in terms of their radiative forcing after  $\text{CO}_2$ . Atmospheric levels of  $\text{CH}_4$  have been increasing globally since 2007, after a period of relative stability from the late 1990s to early 2000s, and is likely due to increasing fossil fuel and anthropogenic microbial sources, such as from agriculture and waste (e.g. (Jackson et al., 2020)). This is of concern, since  $\text{CH}_4$  is a powerful GHG with a global warming potential (GWP) of 81 on a 20-year time horizon. Therefore, there is significant political interest in reducing  $\text{CH}_4$  emissions, e.g. Methane Pledge which aims to reduce  $\text{CH}_4$  emissions globally 30% by 2030. Atmospheric levels of  $\text{N}_2\text{O}$  have been increasing at an accelerating rate since measurements began in the 1990s.  $\text{N}_2\text{O}$  is also a powerful GHG with a GWP of 273 on a 20-year time horizon, and is a long-lived species. Both  $\text{CH}_4$  and  $\text{N}_2\text{O}$  have very uncertain emissions, both from natural and anthropogenic, owing to the important contribution of microbial processes to the emissions, which are complex and depend non-linearly on environmental conditions and are difficult to model.

Atmospheric inverse modelling provides a means to derive estimates of the fluxes of  $\text{CH}_4$  and  $\text{N}_2\text{O}$  based on atmospheric observations, and thus is a useful tool to compare with bottom-up model estimates. However, a main uncertainty in inversion derived fluxes is that due to uncertain atmospheric transport. To establish the uncertainty due to this, ensembles of inversions with different atmospheric transport models are often used. However, these ensembles have been hitherto run with different inversion frameworks, which owing to their complexity makes it difficult to compare the results and to pin-point the cause of the differences between their flux estimates. In VERIFY, a new inversion framework, the Community Inversion Framework (CIF) has been developed (Berchet et al., 2021) which can be interfaced with different atmospheric transport models enable a more direct comparison between results and a better estimation of the uncertainty due to transport.

This deliverable presents the results of inversions for  $\text{CH}_4$  and  $\text{N}_2\text{O}$  using the CIF interfaced with the regional Eulerian model, CHIMERE, and two variants of the Lagrangian model, FLEXPART. The inversions cover the European domain and the common time period 2006 to 2017 and, as far as possible, use the same prior fluxes, atmospheric observations and boundary conditions. The atmospheric models are described in Section 4.1, the prior information and other data inputs are described in Section 4.2, and the individual model set-ups are described in Section 4.3. The results from all inversions are compared and described in Section 4.4.

## 4. Methane and nitrous oxide fluxes from the CIF

### 4.1. Atmospheric transport models

#### 4.1.1. CHIMERE

CHIMERE (see <https://www.lmd.polytechnique.fr/chimere/>) is a non-hydrostatic Eulerian chemistry-transport model. Its area-limited domains can be designed to cover the hemispheric to the urban scales, with horizontal resolutions from several degrees to one kilometer. The time-steps usually cover a few minutes, depending on the CFL and choices made by the user for minimizing computation costs. For the purpose of flux inversions, the tangent-linear and the adjoint codes have been developed and parallelized, only for trace-gases (see (Fortems-Cheiney et al., 2021), their Section 3.2 for more details). The required input data are meteorological 3D and 2D fields (e.g. temperature, wind speed), boundary conditions for concentrations at the four sides and at the top of the domain and emission fluxes. The comparison to surface measurements is done by extracting from the model the simulated concentrations in the grid cell matching the stations' locations for the time-steps matching the measurement date and time. If the measurement covers a longer time (e.g. hourly means), the simulated concentrations for the matching time-steps are averaged. For this deliverable, CHIMERE was run using meteorological data from the ECMWF's IFS operational forecast (every three hours) retrieved at  $0.25^\circ \times 0.25^\circ$  and interpolated onto the model's grid ( $0.5^\circ \times 0.5^\circ$ ). CHIMERE extends from the surface to 200 hPa with 17 sigma-pressure levels.

#### 4.1.2. FLEXPART

FLEXPART is a Lagrangian model, which is driven by external meteorological fields, e.g., ECMWF operational forecast or reanalysis fields (Stohl et al., 2005)(Pisso et al., 2019). FLEXPART can be run in forward time mode, modelling the change in atmospheric mixing ratio due to surface fluxes, or in a backwards time mode, modelling the sensitivity of observations to surface fluxes (also known as observation *footprints*) (Seibert and Frank, 2004). The footprints can be used to derive a matrix operator of atmospheric transport for use in atmospheric inversions (Thompson and Stohl, 2014). FLEXPART can also be run in a domain filling mode, in which the whole atmosphere is filled with millions of virtual particles, which are used to simulate atmospheric transport and mixing ratios (Zwaafink et al., 2018). FLEXPART can account for linear (or near-linear) atmospheric chemistry (e.g. loss due to oxidation by the hydroxyl radical (OH) using pre-calculated OH fields), and wet and dry deposition.

For the inversions provided by NILU, FLEXPART-v10.4 was run using ECMWF's operational IFS forecast with backward trajectory lengths of 10 days for CH<sub>4</sub> and 7 days for N<sub>2</sub>O. The footprints were saved at  $0.25^\circ \times 0.25^\circ$  for CH<sub>4</sub> inversions and  $0.5^\circ \times 0.5^\circ$  for N<sub>2</sub>O inversions.

For the inversions provided by EMPA, FLEXPART-v9.2 was run using ECMWF's ERA-Interim (up to 2018) and ERA5 for 2019 with backward trajectory lengths of 10 days and footprints were saved at  $0.25^\circ \times 0.25^\circ$ .

## 4.2. Input data for inversions

### 4.2.1. Atmospheric observations

Atmospheric observations of CH<sub>4</sub> and N<sub>2</sub>O used in the FLEXPART inversions were the same as used in D4.9 and consisted of surface measurements from flask and continuous sampling sites. The data were compiled from multiple sources:

1. the InGOS project harmonized dataset, which approximately covers the period from 2005 to 2014 (available from <https://www.icos-cp.eu>)
2. the ICOS atmospheric network (<https://www.icos-cp.eu>)
3. the World Data Centre for Greenhouse Gases (WDCGG, <https://gaw.kishou.go.jp>)
4. the NOAA ESRL discrete sampling network (<https://www.esrl.noaa.gov/gmd/>)
5. the EBAS data base (<http://ebas.nilu.no>)
6. personal communications of data from station principle investigators

The dataset consisted of 27 sites for CH<sub>4</sub> and 22 sites for N<sub>2</sub>O, that is sites with data covering at least 9 years between 2005 and 2019. This dataset is referred to as the "VERIFY core" dataset. The aim of this selection is to avoid as much as possible the impact of changes in the network of observations on the inter-annual variability of the retrieved fluxes. Data from sites with continuous measurements were averaged to hourly values. The sites are shown in Figure 1.

### 4.2.2. Prior fluxes

The prior fluxes were the same as those used in D4.9. For CH<sub>4</sub>, these estimates were prepared from D4.3 for anthropogenic emissions (EDGAR-v6) and D4.6 for fluxes from natural soils (JSBACH-HIMMELI) and inland waters (CSLM-CH<sub>4</sub> model), and were supplemented by estimates from previous studies for geological, ocean and termite emissions (see Table 1). For D4.3, the EDGAR estimates were updated to include new activity data for 2016 to 2018, whereas in the previous version emissions for these years were based on a so-called *fast-track* estimation using proxies. For D4.6, the new estimate for lakes combines an empirical estimate, which provides only an annual climatology, with a monthly-resolved estimate from a mechanistic-stochastic modelling approach (MSM) accounting for nutrient (N and P) loads delivered to each lake and control of CH<sub>4</sub> emission by the lake trophic status (see D4.6 for details).

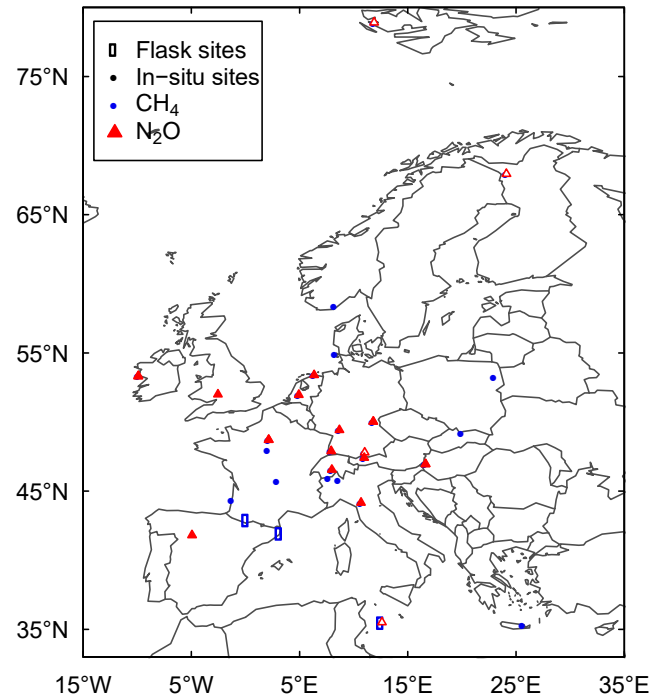


Figure 1. Map of sites in the VERIFY core dataset.

Table 1: Overview of the prior CH<sub>4</sub> flux estimates

Source	Reference	Global total (Tg/y)	EU27 + UK total (Tg/y)
Agriculture and waste <sup>1</sup>	EDGAR-v6	227.1	15.9
Fossil fuels <sup>1</sup>	EDGAR-v6	115.6	3.9
Biofuels and biomass burning <sup>1</sup>	EDGAR-v6 (biofuel) and GFED-v41s (biomass)	27	0.81
Geological <sup>2</sup>	(Etiope et al., 2019)	15.0	2.7
Termites	(Saunois et al., 2020) (GCP-CH <sub>4</sub> )	8.9	0.10
Ocean	Weber et al. 2019	9.4	0.01
Mineral soils	JSBACH-HIMMELI	116.3	0.15
Soil sink	JSBACH-HIMMELI	-42.8	-1.1
Peatlands	JSBACH-HIMMELI	15.2	0.9
Inundated	JSBACH-HIMMELI	38.1	1.07
Lakes <sup>3</sup>	ULB model	0.52	0.2
<b>Total</b>		<b>530.3</b>	<b>24.6</b>

<sup>1</sup>EDGAR-v6 is only up to 2018 so estimates for 2019 were made by repeating the 2018 estimate

<sup>2</sup>These estimates were scaled to a global total of 15 Tg/y consistent with (Petrenko et al., 2017)

<sup>3</sup>These estimates are only available for Europe

For N<sub>2</sub>O anthropogenic emissions were taken from EDGAR-v6 (D4.3). An estimate for the natural N<sub>2</sub>O flux was provided by the O-CN land surface model – a monthly climatology of the pre-industrial (or *baseline*) fluxes (Zaehle et al., 2011) and an estimate for the ocean N<sub>2</sub>O flux was provided by the coupled ocean-biogeochemistry model, PlankTOM-v10 – also a monthly climatology (Buitenhuis et al., 2018). (See Table 2).

**Table 2: Overview of the prior N<sub>2</sub>O flux estimates**

Source	Reference	Global total (Tg/y)	EU27 + UK total (Tg/y)
Agriculture <sup>1</sup>	EDGAR-v6	6.30	0.59
Waste, fuel combustion and industry <sup>1</sup>	EDGAR-v6	2.79	0.28
Biomass burning	GFED-v41s	0.67	0.0005
Natural soils	O-CN	5.94	0.08
Ocean	PlankTom-v10	2.59	0.0
<b>Total</b>		<b>18.3</b>	<b>0.95</b>

### 4.2.3. Boundary conditions

The models used in the inversions covered only a spatially limited domain, i.e., 15°W to 35°E and 33°N to 73°N, and in addition, the Lagrangian model, FLEXPART covers only a limited temporal domain as defined by the duration of the backward trajectories. Therefore, it was necessary to provide boundary mixing ratios. These were provided by the CAMS v19 reanalysis mixing ratios fields for CH<sub>4</sub> and N<sub>2</sub>O.

For FLEXPART simulations a so-called background mixing ratio is computed for each observation, which takes into account the contribution from variations in mixing ratios not covered by the limited spatial and/or temporal coverage of the backward simulations. For the NILU simulations, the background was calculated by coupling the termination points of the virtual particles to the initial mixing ratios from CAMS and taking a weighted mean of these, and additionally, the contribution to the mixing ratio from fluxes outside the inversion domain (also from CAMS) was calculated by integrating these with the footprints outside of the domain following (Thompson and Stohl, 2014). For the EMPA simulations, background mixing ratios were taken from CAMS simulations following the two-step approach for nested global and regional inversions (Rödenbeck et al. 2009). For this, an additional global CAMS simulation was conducted, in which emissions were only released over the European domain (15°E to 35°W, 35°N to 70°N) and tracers were terminated as soon as they left this domain. Background mixing ratios were then obtained by subtracting CH<sub>4</sub> from this European simulation from the regular CAMS run. Differences in background mixing ratios obtained with the particle position approach and the Rödenbeck approach were recently analyzed by Bergamaschi et al. (2022). Background mixing ratios from the

particle position approach were on average slightly higher, which resulted in somewhat lower emissions (e.g. -7% over Germany, -13% over France) compared to the Rödenbeck approach.

### 4.3. Inversion set-up

#### 4.3.1. Control vector

The control vector contains the variables to be optimized in the inversion, and in this case, the variables that are applied to the prior fluxes (and boundary conditions) to obtain the posterior fluxes.

**Table 3: Overview of the control vector variables**

Variable	CHIMERE	FLEXPART	FLEXPART-EMPA
Flux spatial resolution	0.5° × 0.5°	0.25° × 0.25° for CH <sub>4</sub> 0.5° × 0.5° for N <sub>2</sub> O	0.25° × 0.25°
Flux temporal resolution	Daily	Monthly	Monthly
Boundary conditions	<ul style="list-style-type: none"> <li>Scalars of initial mixing ratios at model resolution</li> <li>Scalars of lateral boundary mixing ratios every 2 days</li> <li>Scalars of top boundary mixing ratios every 2 days</li> </ul>	<ul style="list-style-type: none"> <li>Scalars of mixing ratios for 4 latitudinal bands globally and for each month</li> </ul>	Not optimized

#### 4.3.2. Uncertainties

The uncertainties for the prior fluxes and observations need to be set in the inversions and are important for determining how strongly the posterior fluxes are tied to the prior. The larger the uncertainties on the prior fluxes, the more degrees of freedom the inversion has to match to the observations. The smaller the uncertainties on the difference between the observed and modelled mixing ratios, the closer the inversion tries to match the observations by adjusting the control variables (and hence fluxes). In the CIF, the uncertainties are described by matrices, with variances on the diagonal and covariances on the off-diagonal. They are called respectively the prior error (for the error statistics on the prior controlled variables) and the observation error (for the error statistics on the difference between the observed and modelled mixing ratios). Table 4 shows the main characteristics of the prior error covariance matrices for each inversion set-up.

**Table 4: Overview of the control vector variables**

	CHIMERE	FLEXPART	FLEXPART-EMPA
Prior flux uncertainty (SD)	100% of prior flux in each grid cell	50% of prior flux in each grid cell	100% of prior flux in each grid cell
Flux spatial correlation length	200 km over land 1000 km over sea	200 km over land 1000 km over sea	100 km over land and ocean

Flux temporal correlation length	2500 hours	2160 hours	2 years
Initial mixing ratios	100% and correlation length of 1000 km	0.1%	N/A
Lateral boundary mixing ratios	100% and correlations of 1000 km and 5 days	N/A	N/A
Top boundary mixing ratios	100% and correlations of 5 days	N/A	N/A

Observations errors were assumed to be independent from each other in all inversions, i.e., the observation error covariance matrix is diagonal. The observation errors were determined in each inversions as follows:

- CHIMERE: Computed from the measurement error (where available) from the provided observation files. For CH<sub>4</sub> these errors were combined with the transport, representation, and aggregation errors calculated for each station following (Szénási et al., 2021) using simulations based on the TNO emission inventory. For N<sub>2</sub>O, measurement errors were provided from observation files. Transport, representation and aggregation errors were deduced from the CH<sub>4</sub>-based errors.
- FLEXPART: For CH<sub>4</sub> these were taken from the observation files, but set to a minimum of 9 ppb. In addition, 50% of the contribution to from the fluxes outside the inversion domain (used in the calculation of the background mixing ratio) was added to the observation error. For N<sub>2</sub>O, the observations errors were calculated in the same way as for CH<sub>4</sub> but a minimum error of 0.3 ppb was used.
- FLEXPART-EMPA: Measurement errors were composed of an observation error and a model error, which are summed quadratically to obtain the total error. Observation errors were taken from the observation files and an average model error was determined for each station separately by an iterative procedure, following Koohkan and Bocquet (2012): An initial value was computed from the root-mean-square-differences between a priori simulated values and the observations. With this initial value, an inversion was performed. The model error was then scaled using the Eq. (20) of Koohkan and Bocquet (2012) until convergence.

## 4.4. Results

### 4.4.1. Methane mixing ratios

A comparison of the prior and posterior simulated mixing ratios is provided at three example sites to illustrate how well the different atmospheric transport models capture the variability in the observations (Figure 2). Data are compared for the common inversion period of 2006 to 2017, although the FLEXPART inversions were run up to 2019. The FLEXPART simulations from NILU have a positive bias in the prior simulated mixing ratio at a number of mountain sites, namely Monte Cimone (CMN), Jungfraujoch (JFJ), Puy de Dôme (PUY) and Zugspitzschneefernerhaus (ZSF), which is most likely due to the particle releases in the Lagrangian model being at a too low height, which can occur if the observation height is given in meters above ground level since the model topography has finite model resolution and is smoothed-out compared to the reality. These shortcomings will be addressed in future simulations.

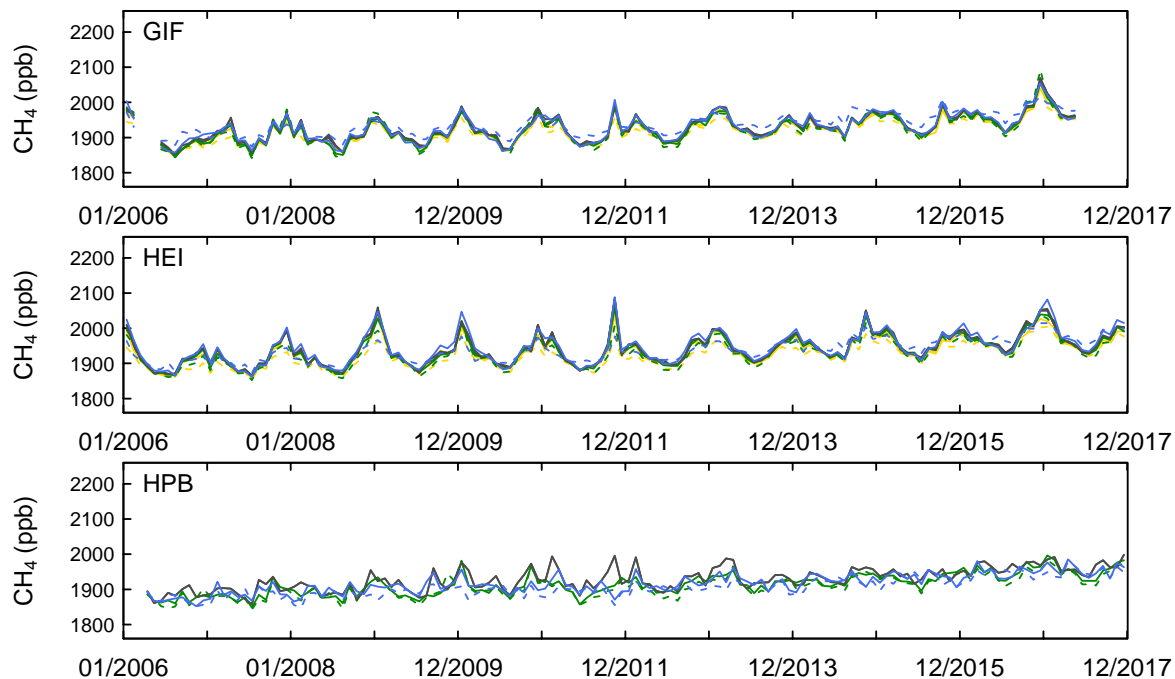


**Figure 2. Monthly mean CH<sub>4</sub> mixing ratios at Gif-sur-Yvette (GIF), Heidelberg (HEI) and Hohenpeissenberg (HPB) sites simulated with the 3 models (CHIMERE = blue, FLEXPART = yellow, FLEXPART-EMPA = green, observation = grey) the prior is shown with the dashed line and the posterior the solid line.**

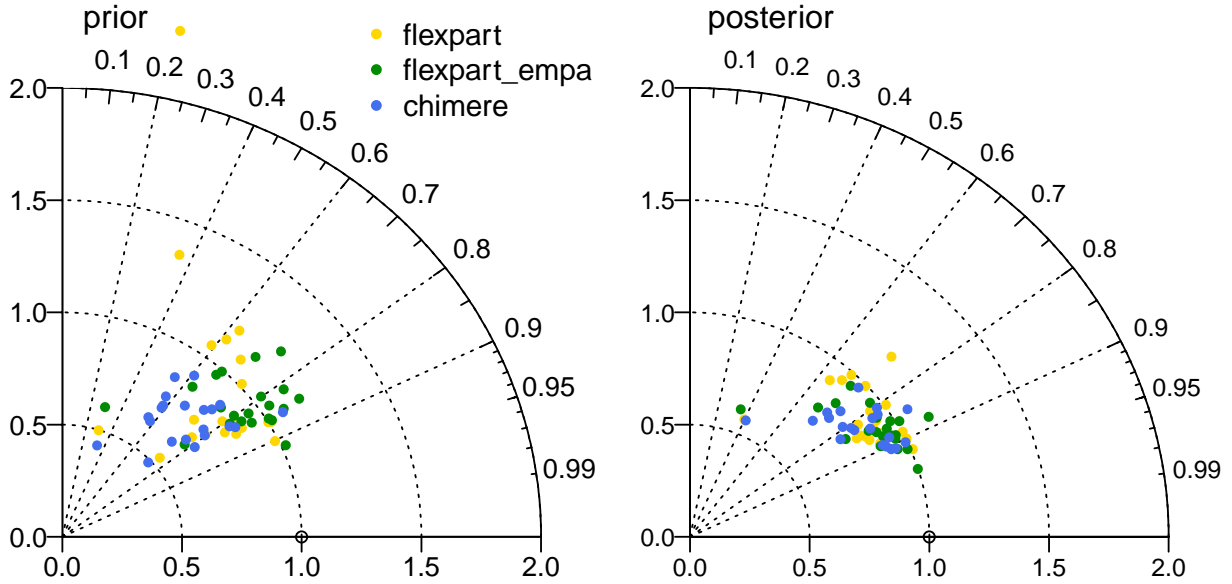


Figure 3. Taylor diagrams showing the correlation (angle) and normalized standard deviation (radius) between simulated and observed CH<sub>4</sub> mixing ratios at all sites (left: using the prior fluxes, right: using the posterior fluxes).

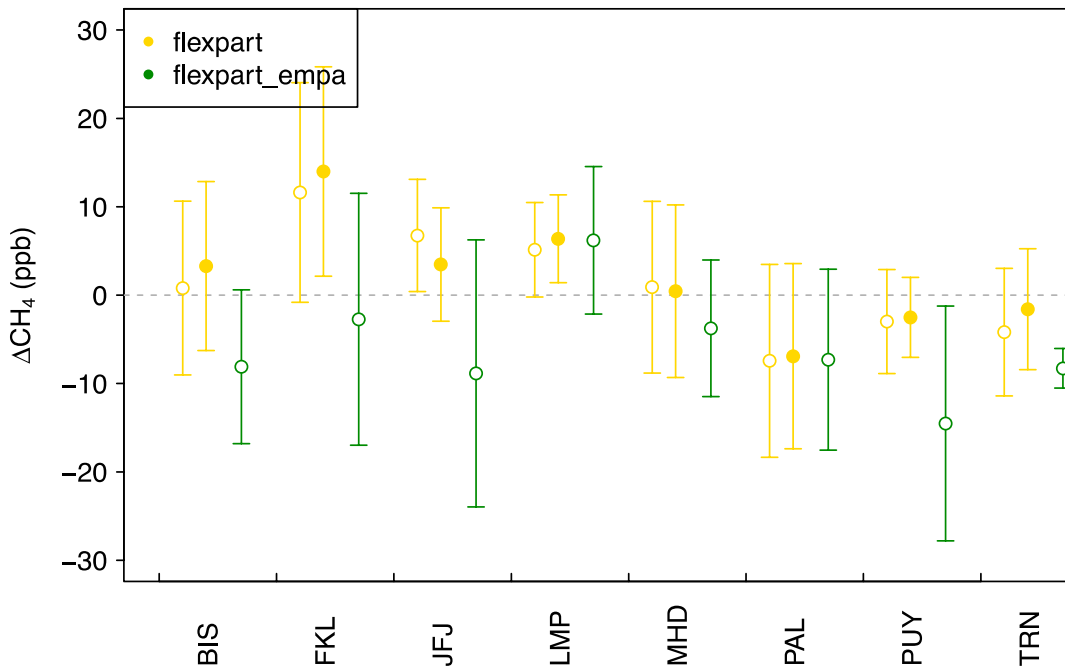


Figure 4. Bias in background mixing ratio compared to observations for times with little in-domain influence. Only sites with more than 10 instances of background conditions are shown (open circles: prior, solid circles: posterior). Note, the background was not optimized in FLEXPART-EMPA.

Figure 3 compares the prior and posterior correlations and normalized standard deviations (NSD) of the simulated and observed mixing ratios for each site and atmospheric transport model (only

sites common to all inversion frameworks are shown). CHIMERE gives a somewhat lower NSD compared to the two FLEXPART simulations, possibly owing to the coarser resolution. All inversions result in a better match between the observed and simulated mixing ratios with the posterior fluxes, as expected. Table 5 shows the root-mean-square-errors (RMSE) for the prior and posterior mixing ratios compared to the observations (RMSE was calculated only using sites common to all inversion frameworks).

Table 5. Root mean square error (RMSE) of prior and posterior CH<sub>4</sub> mixing ratios versus observations for all sites common to all inversion frameworks.

	CHIMERE	FLEXPART	FLEXPART-EMPA
<b>Prior</b>	38.6	44.9	34.9
<b>Posterior</b>	30.0	29.7	28.0

For the inversions using FLEXPART, the background mixing ratios were also provided and are compared in Figure 4. Biases in the background mixing ratio were estimated by looking for observations times when the modelled contribution to the mixing ratio from fluxes inside the domain was less than 4 ppb, these are from hereon referred to as background conditions. The mean bias (simulated background minus observed mixing ratio) was calculated for all years for sites where both NILU and EMPA simulations found at least 10 instances of background conditions. The biases were 0.1 ppb and -5.7 ppb in the NILU and EMPA simulations, respectively.

#### 4.4.2. Methane fluxes

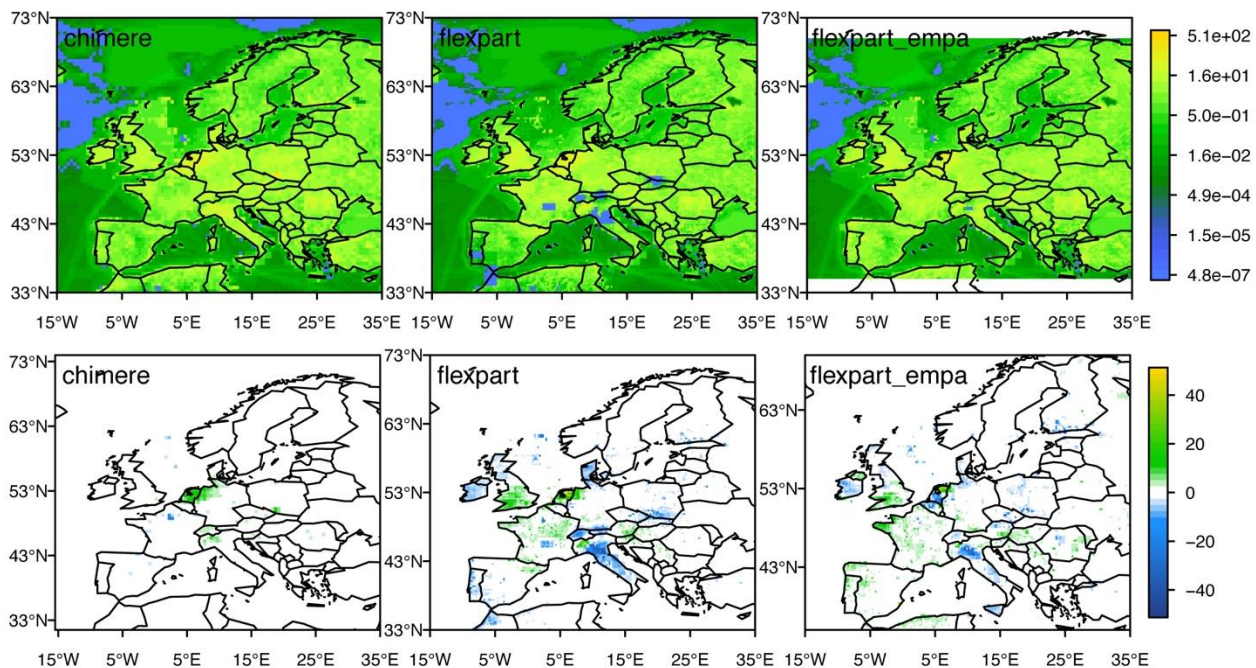


Figure 5. Posterior fluxes averaged over 2015-2017 ( $\text{g m}^{-2} \text{y}^{-1}$ ) shown with a log base 2 colour scale (top) and the flux increments ( $\text{g m}^{-2} \text{y}^{-1}$ ) shown on a linear colour scale.

Figure 5 shows the posterior  $\text{CH}_4$  fluxes and flux increments from each of the inversions for the mean of the years 2015-2017. The pattern of  $\text{CH}_4$  fluxes are broadly similar between the 3 inversions with high emissions in the Netherlands and Belgium, western France and southern UK. However, FLEXPART NILU inversions show some spurious areas of very low fluxes in Italy, Switzerland and southern France, which are presumably owing to the positive bias in the prior modelling mixing ratios at mountain sites (CMN, JFJ, PUY, and ZSF) mentioned above. The patterns of flux increments (posterior minus prior fluxes) is, however, quite different between the CHIMERE and two FLEXPART inversions. All inversions find positive increments (posterior higher than prior) over northern Netherlands, but FLEXPART-EMPA finds negative increments over southern Netherlands. Also, both FLEXPART inversions find negative increments over northern Italy, which is not the case in CHIMERE.

Figure 6 shows the area integrated fluxes (emissions) for EU27 plus UK, Switzerland and Norway (EU27+3), northern, western, central and southern Europe averaged for each year. CHIMERE has slightly larger emissions for EU27+3, compared to the two FLEXPART inversions. For EU27+3, the total mean emissions were 26, 22 and 24 Tg  $\text{CH}_4/\text{y}$ , for CHIMERE, FLEXPART-NILU and FLEXPART-EMPA, respectively. The two FLEXPART inversion results are very similar for most regions in terms of the magnitude and multi-annual trends. The one region where they do differ notably is in southern Europe where the NILU inversion shows much lower emissions. The approximately 2 Tg  $\text{CH}_4/\text{y}$  difference between the NILU and EMPA inversions for EU27+3 emissions is likely owing to small differences in the boundary conditions (Figure 7) and to the too low model heights in the NILU simulations for mountain sites as discussed above.

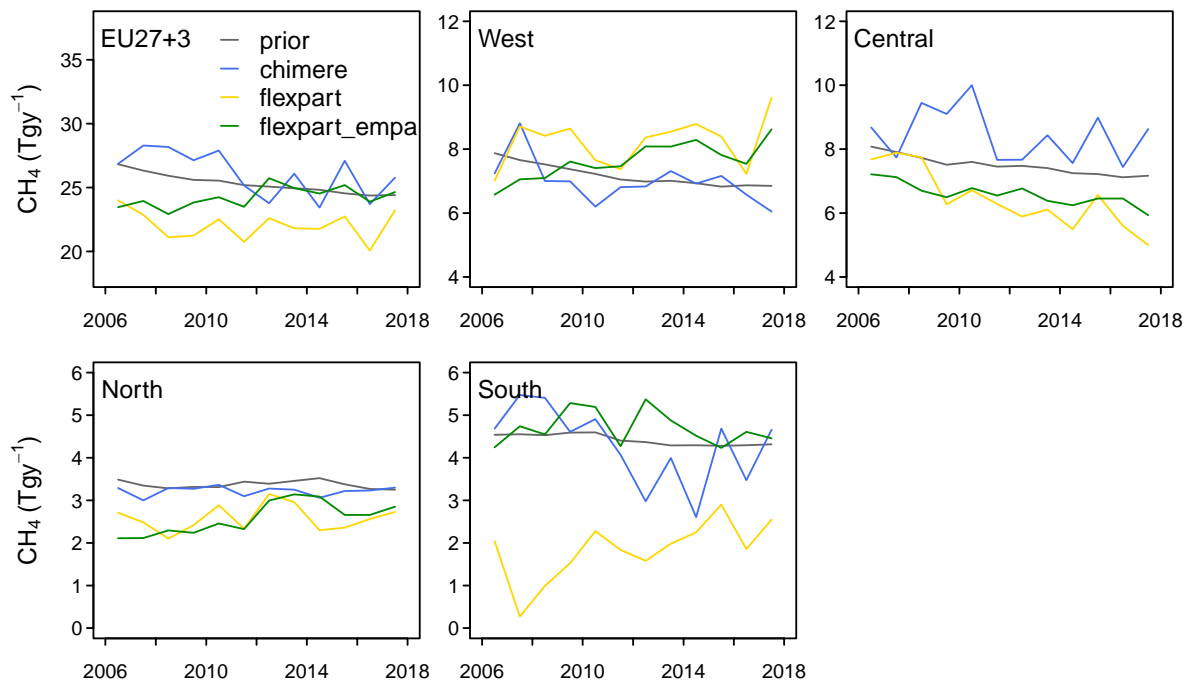


Figure 6. Annual mean area integrated fluxes (Tg/y) for each inversion and the prior

Figure 7 shows the total emission for EU27+3 versus the annual mean bias between the observed and modelled background mixing ratios. As expected, there is a negative correlation, that is, the greater the underestimate in background mixing ratio the larger the fluxes in the inversion domain are to compensate.

Figure 8 shows the mean seasonal cycle in the area integrated fluxes for EU27+3, northern, western, central and southern Europe. The prior fluxes indicate a summer maximum in EU27+3 and northern Europe with almost no seasonality in the other regions. The two FLEXPART inversions show similar seasonality to the prior, with the exception that they indicate a small summer maximum in the western and central European regions as well, and the NILU inversion indicates a secondary maximum in February. CHIMERE, on the other hand, produces a very different seasonality with summer minimum for all regions except northern Europe, which is unexpected and is likely due to one or more of the following: a misrepresentation of the atmospheric transport, errors in the seasonality of OH loss, or poor representation of the boundary conditions,

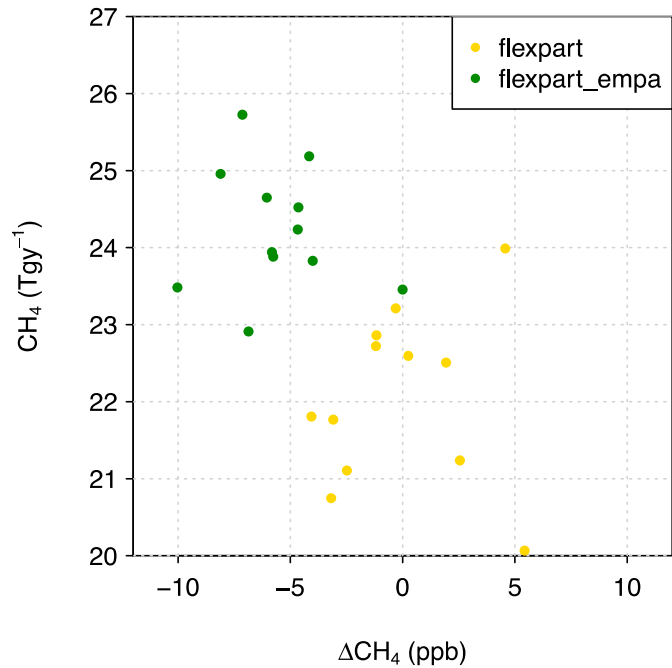
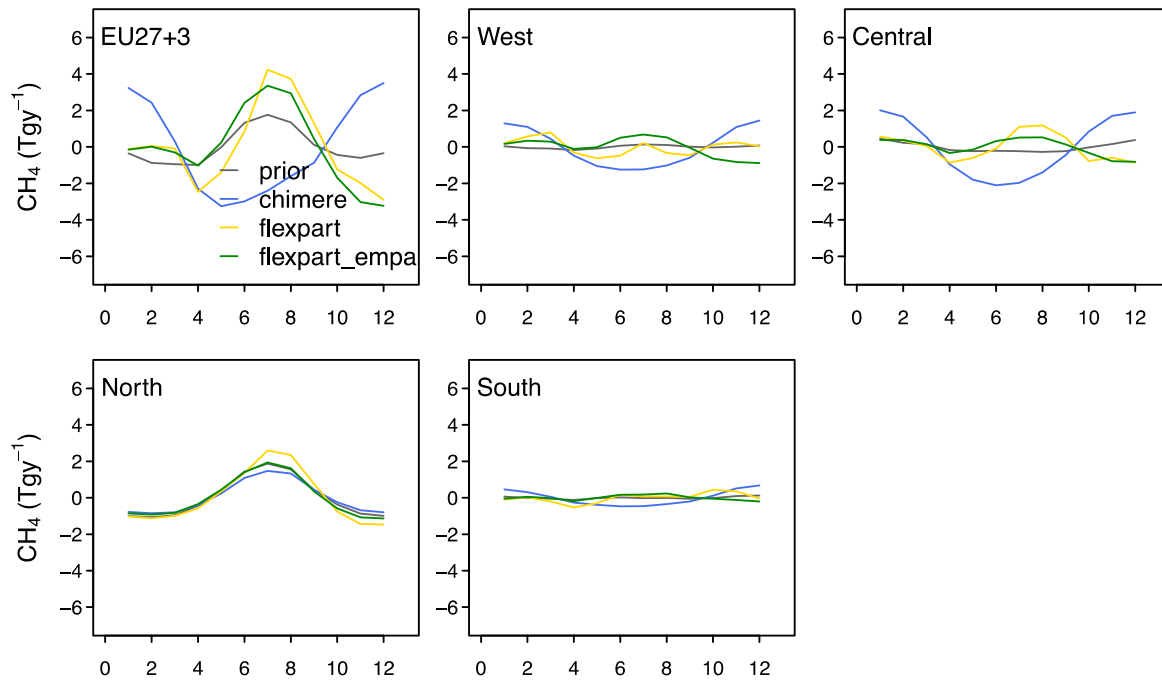


Figure 8. Annual emissions for EU27+3 versus the annual bias in the background mixing ratios for the FLEXPART NILU and EMPA inversions.

Figure 7. Mean seasonal cycles in the area integrated fluxes (Tg/y) for each inversion and the prior.

and requires further investigation.



#### 4.4.3. Nitrous oxide mixing ratios

A comparison of the prior and posterior simulated mixing ratios and observations is shown at three example sites for the two models that ran N<sub>2</sub>O inversions, CHIMERE and FLEXPART (Figure 9). Data are compared for the common inversion period of 2005 to 2018, although the FLEXPART inversions were run up to 2019.

The prior simulation with FLEXPART captures the observed variability of N<sub>2</sub>O already very well with correlations at all sites of at least 0.8 (see Figure 10). However, the prior fluxes lead to FLEXPART generally underestimating the mixing ratios at a number of sites, i.e., Cabauw (CBW), Gif sur Yvette (GIF), Heidelberg (HEI) and Lutjewad (LUT). The prior simulation of CHIMERE is slightly poorer at capturing the observed variability with correlations of at least 0.65 and generally NSD generally greater than one (Figure 10).

For the inversions using FLEXPART, the background mixing ratios were also provided and are compared in Figure 11. Similar to the CH<sub>4</sub> inversions, biases in the background mixing ratio were estimated by looking for observations times when the modelled contribution to the mixing ratio from fluxes inside the domain was less than 4 ppb. The mean bias (prior simulated background minus observed mixing ratio) calculated for all years for sites where there were at least 10 instances of background conditions was -0.37 ppb but with a slightly more negative bias prior to 2013.

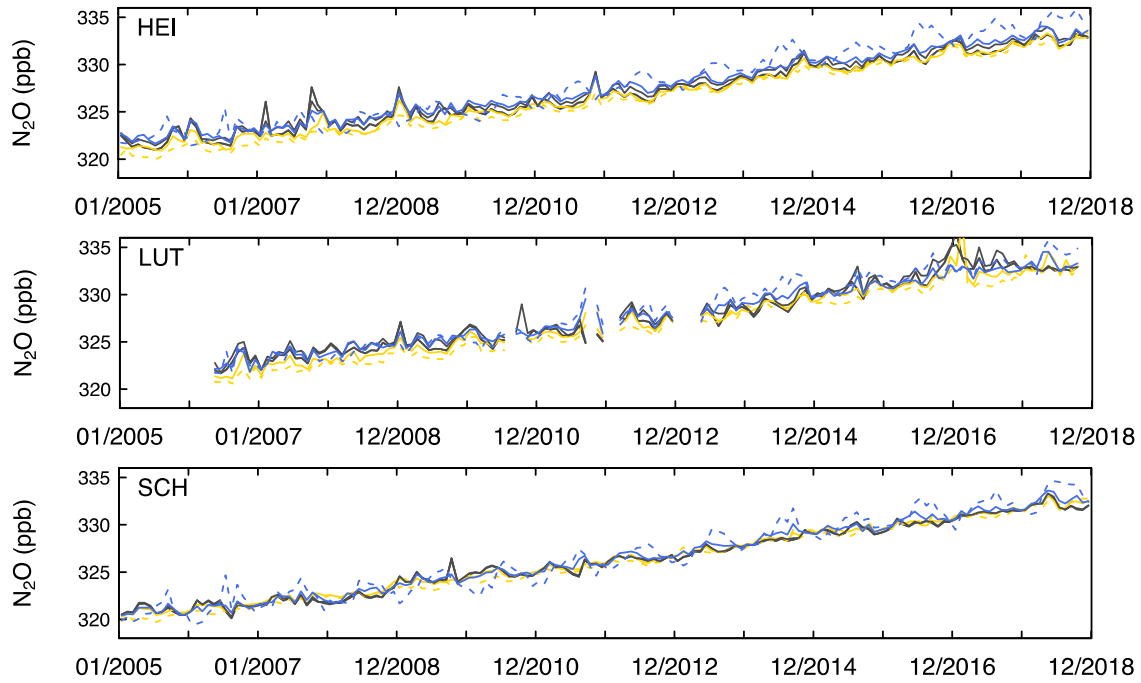


**Figure 9. Monthly mean N<sub>2</sub>O mixing ratios at Heidelberg (HEI), Lutjewad (LUT) and Schauinsland (SCH) sites simulated with the 2 models (CHIMERE = blue, FLEXPART = yellow, observation = grey) the prior is shown with the dashed line and the posterior the solid line.**

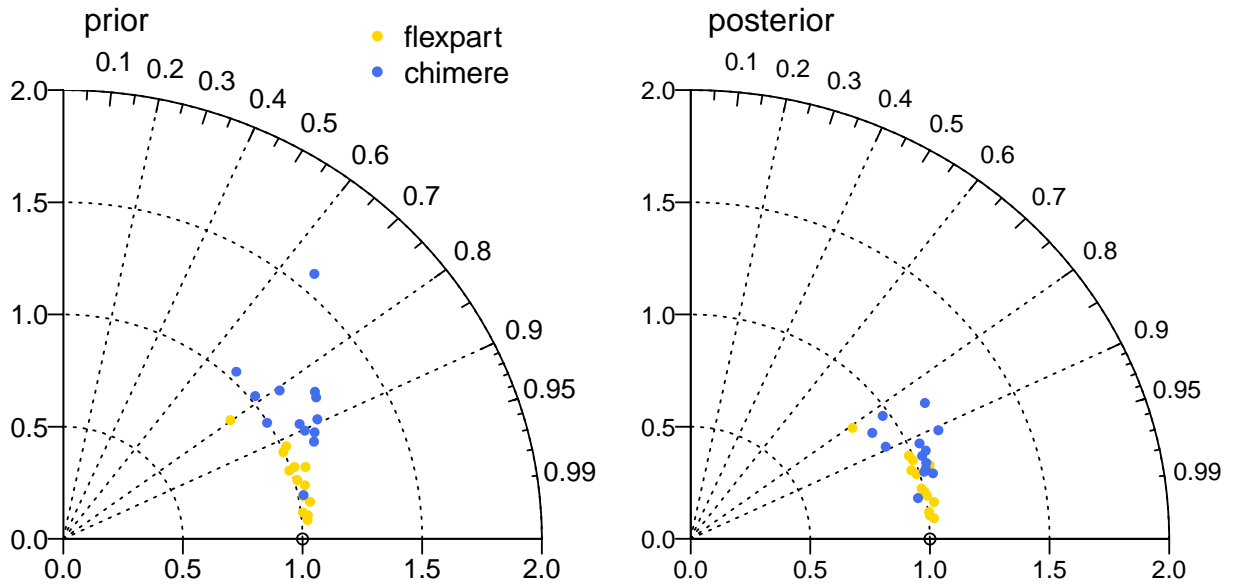


Figure 10. Taylor diagrams showing the correlation (angle) and normalized standard deviation (radius) between simulated and observed CH<sub>4</sub> mixing ratios at all sites (left: using the prior fluxes, right: using the posterior fluxes).

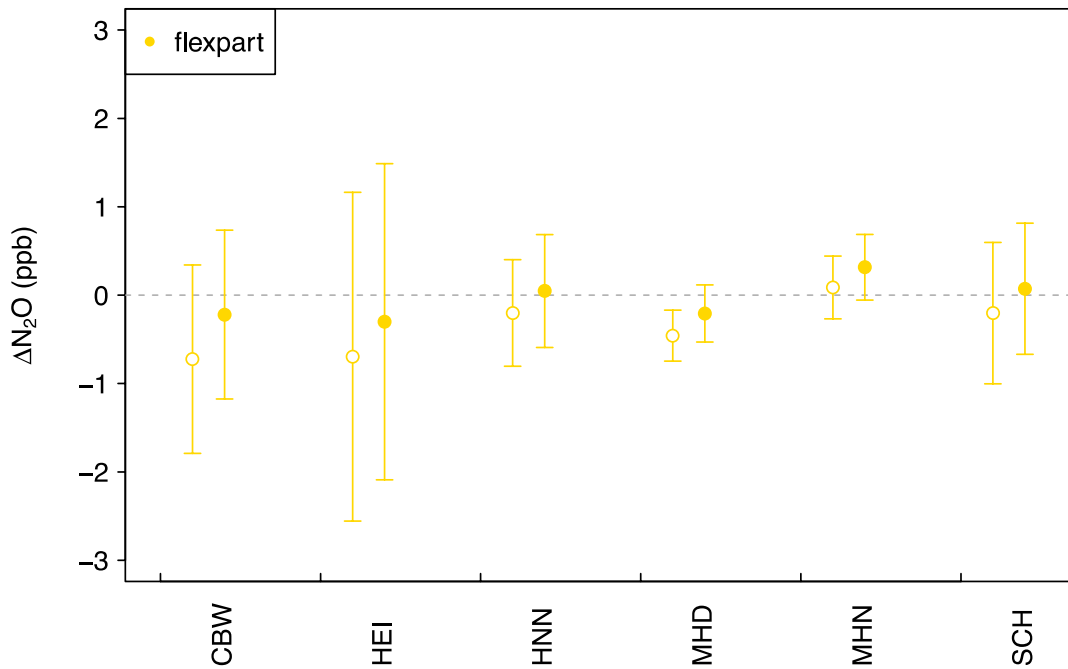
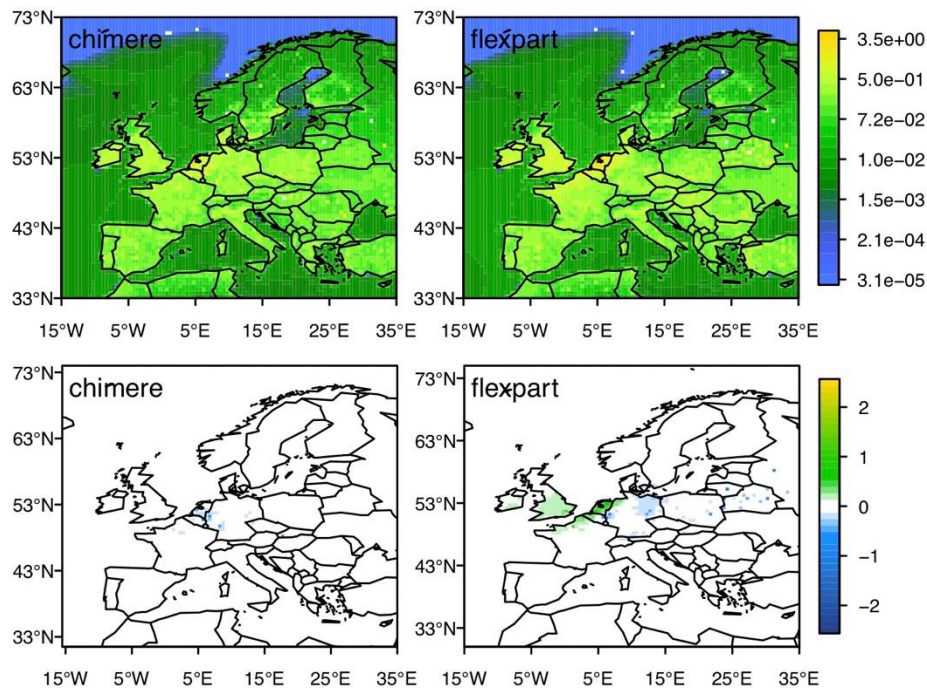


Figure 9. Bias in background mixing ratio compared to observations for times with little in-domain influence. Only sites with more than 10 instances of background conditions are shown (open circles: prior, solid circles: posterior).

#### 4.4.4. Nitrous oxide fluxes

Figure 12 shows the posterior  $N_2O$  fluxes and flux increments from each of the inversions for the mean of the years 2015-2017. The FLEXPART inversion results in slightly larger fluxes over Europe compared to the CHIMERE inversion, especially over the Netherlands, Belgium, northern France and England. In these regions, FLEXPART also results in larger fluxes compared to the prior. On the otherhand, FLEXPART estimates smaller fluxes compared to the prior and to CHIMERE in northeastern Germany. The overall increase in the fluxes compared to the prior in the FLEXPART inversion is consistent with the observation that the prior simulations underestimate the mixing ratios at a number of sites (see Section 4.4.3). The CHIMERE inversion, on the other hand, remains relatively close to the prior fluxes both in magnitude and spatial distribution. The area integrated mean flux for EU27+3 for the period 2005-2018 is 0.98 and 1.07 TgN/y for CHIMERE and FLEXPART, respectively, compared to the prior estimate of 0.98 TgN/y.

Figure 13 shows the area integrated fluxes for EU27+3 countries as well as for northern, western, central and southern Europe averaged for each year. At the EU level, the two inversions agree quite well for the overall magnitude of the emissions as well as for the inter-annual trend, which decreases by 0.010 TgN/y and 0.019 TgN/y per year for CHIMERE and FLEXPART, respectively. The decrease at EU level is driven by decreases in western and central Europe, while there is little



change in emissions in northern and southern Europe.

**Figure 12.** Posterior fluxes averaged over 2015-2017 ( $g\ m^{-2}\ y^{-1}$ ) shown with a log base 2 colour scale (top) and the flux increments ( $g\ m^{-2}\ y^{-1}$ ) shown on a linear colour scale.

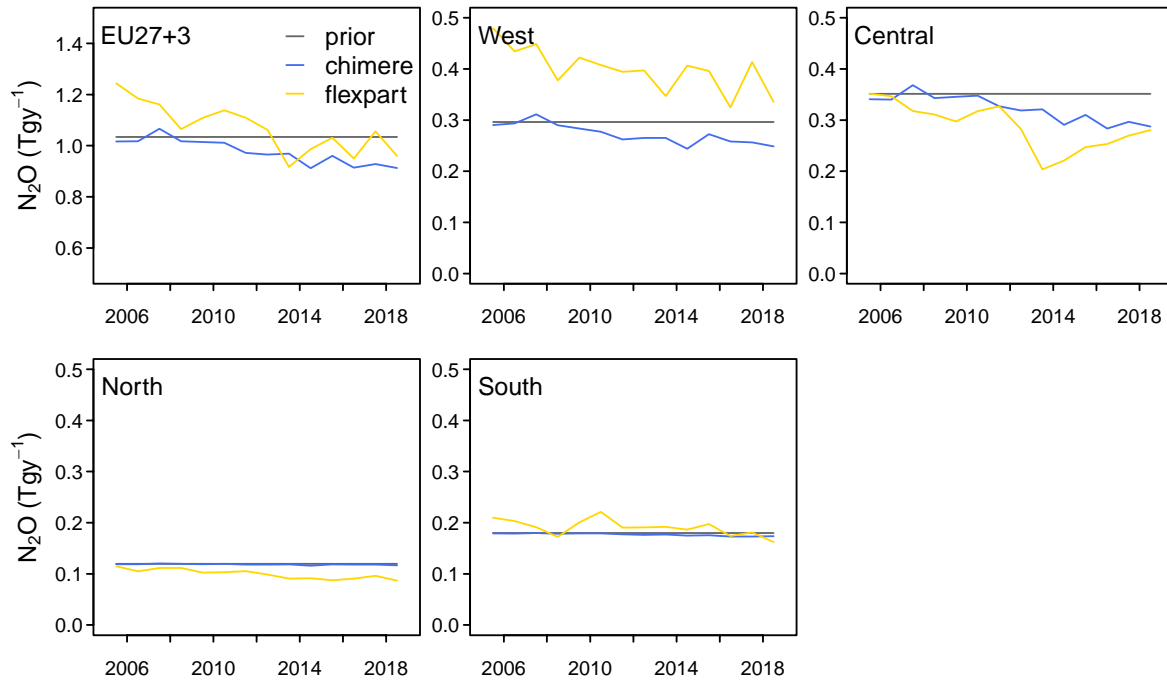


Figure 13. Annual mean area integrated fluxes (TgN/y) for each inversion and the prior

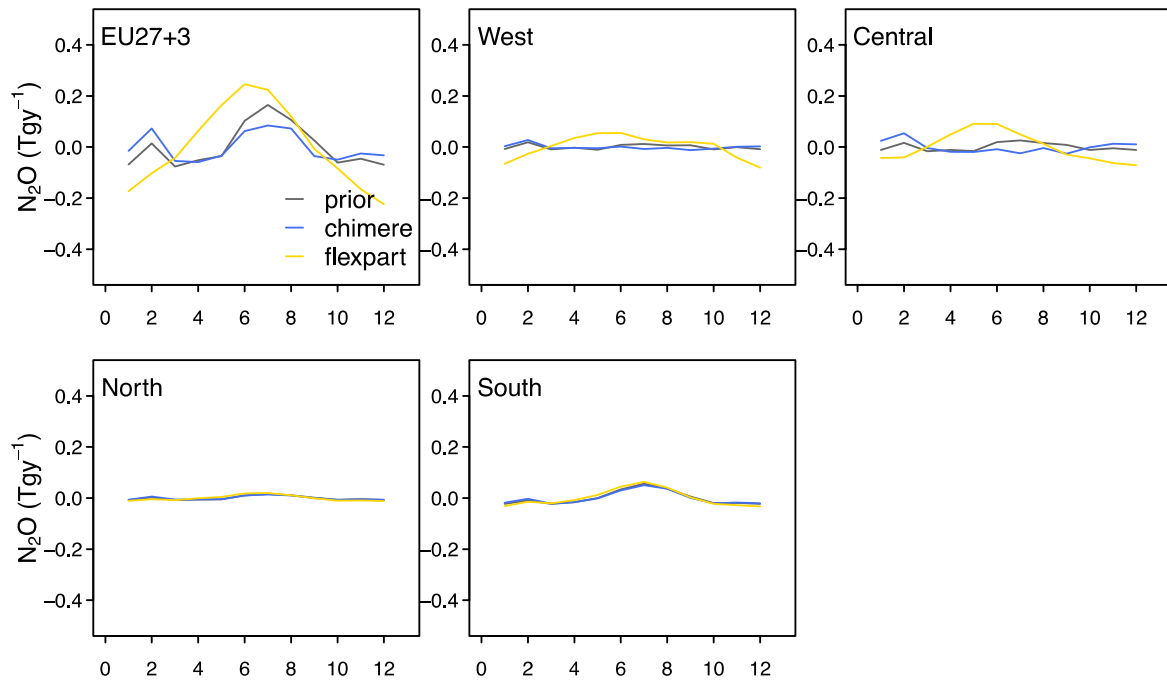
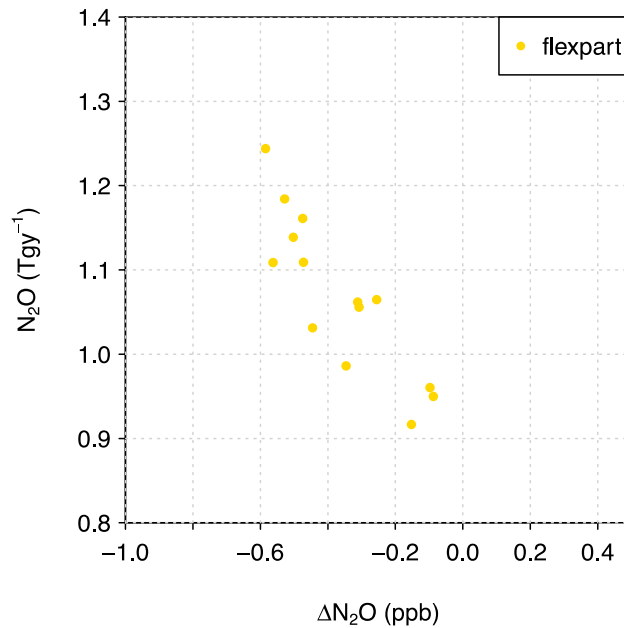


Figure 14. Mean seasonal cycles in the area integrated fluxes (TgN/y) for each inversion and the prior

Figure 14 shows the seasonal cycle for EU27+3 countries as well as for western, central, northern and southern Europe. The flux seasonal cycle for EU27+3 from CHIMERE remains very close to that of the prior estimate with a weak maximum in July and a secondary maximum in February. FLEXPART, on the other hand, shows no secondary winter maximum, and the summer maximum occurs one month earlier in June. The seasonal cycles in western and central Europe are similar to that for EU27+3. For northern and southern Europe both inversions remain very close to the prior estimate most likely because these regions are less well constrained by observations thus there are fewer degrees of freedom of signal.



**Figure 15. Annual emissions for EU27+3 versus the annual bias in the background mixing ratios for the FLEXPART inversion.**

Finally, Figure 15 shows the total emission for EU27+3 versus the annual mean bias between the observed and modelled background mixing ratios for FLEXPART. Similar to CH<sub>4</sub>, there is a negative correlation, that is, the greater the underestimate in background mixing ratio the larger the fluxes in the inversion domain are to compensate. A rough estimate of the sensitivity of the fluxes determined by the inversion for EU27+3 is 0.5 TgN/y per ppb of bias in the background mixing ratio. This highlights the need for very accurate background mixing ratio estimates.

## 5. Conclusions

In VERIFY, a new inversion framework, the Community Inversion Framework (CIF), was developed which is a Python-based set of atmospheric inversion tools (Berchet et al. 2021). The CIF can be interfaced with different atmospheric transport models. This is an important set forward in quantifying the systematic uncertainties associated with atmospheric inversions, as it allows a more direct comparison for the influence of atmospheric transport, resolution, and choice of prior and observation uncertainties on the posterior fluxes.

This deliverable presents the results of inversions for CH<sub>4</sub> and N<sub>2</sub>O using the CIF interfaced with the regional Eulerian model, CHIMERE, and two variants of the Lagrangian model, FLEXPART as used at NILU and EMPA. The inversions cover the European domain and the common time period 2006 to 2017 (for CH<sub>4</sub>) and 2005-2018 (for N<sub>2</sub>O) and, as far as possible, use the same prior fluxes, atmospheric observations and boundary conditions.

For CH<sub>4</sub>, inversions were run with all 3 atmospheric transport models. CHIMERE differed somewhat from the two FLEXPART models, in particular in where the posterior fluxes departed from the prior estimates, and in the posterior seasonal cycle. However, the three models gave reasonably comparable results for the annual emissions at regional scales. For EU27+3, the total mean emissions were 26, 22 and 24 Tg CH<sub>4</sub>/y, for CHIMERE, FLEXPART and FLEXPART-EMPA, respectively.

For N<sub>2</sub>O, inversions were run with CHIMERE and FLEXPART (NILU). The results using the two models were very comparable at the level of EU27+3 with annual mean emissions for 2005-2018 of 0.98 and 1.07 TgN/y and with decreasing trends of 0.010 and 0.019 TgN/y per year for CHIMERE and FLEXPART, respectively.

For both CH<sub>4</sub> and N<sub>2</sub>O results with the FLEXPART model (NILU and EMPA results) highlighted the dependency of the fluxes for a regional domain on the background mixing ratios used in the inversion. This is not a new discovery, but the sensitivity for CH<sub>4</sub> and N<sub>2</sub>O for EU27+3 to biases in the background mixing ratio were better defined with a sensitivity of approximately 0.3 Tg/y per ppb bias for CH<sub>4</sub> and 0.5 TgN/y per ppb bias for N<sub>2</sub>O.

## 6. References

Berchet, A., Sollum, E., Thompson, R. L., Pison, I., Thanwerdas, J., Broquet, G., Chevallier, F., Aalto, T., Berchet, A., Bergamaschi, P., Brunner, D., Engelen, R., Fortems-Cheiney, A., Gerbig, C., Zwaafink, C. D. G., Haussaire, J.-M., Henne, S., Houweling, S., Karstens, U., Kutsch, W. L., Lujckx, I. T., Monteil, G., Palmer, P. I., Peet, J. C. A. van, Peters, W., Peylin, P., Potier, E., Rödenbeck, C., Saunois, M., Scholze, M., Tsuruta, A., and Zhao, Y.: The Community Inversion Framework v1.0: a unified system for atmospheric inversion studies, *Geosci Model Dev*, 14, 5331–5354, <https://doi.org/10.5194/gmd-14-5331-2021>, 2021.

Bergamaschi, P., Karstens, U., Manning, A. J., Saunois, M., Tsuruta, A., Berchet, A., Vermeulen, A. T., Arnold, T., Janssens-Maenhout, G., Hammer, S., Levin, I., Schmidt, M., Ramonet, M., Lopez, M., Lavric, J., Aalto, T., Chen, H., Feist, D. G., Gerbig, C., Haszpra, L., Hermansen, O., Manca, G., Moncrieff, J., Meinhardt, F., Necki, J., Galkowski, M., O'Doherty, S., Paramonova, N., Scheeren, H. A., Steinbacher, M., and Dlugokencky, E.: Inverse modelling of European CH<sub>4</sub> emissions during 2006-2012 using different inverse models and reassessed atmospheric observations, *Atmos Chem Phys*, 18, 901–920, <https://doi.org/10.5194/acp-18-901-2018>, 2018.

Bergamaschi, P., Segers, A., Brunner, D., Haussaire, J.-M., Henne, S., Ramonet, M., Arnold, T., Biermann, T., Chen, H., Conil, S., Delmotte, M., Forster, G., Frumau, A., Kubistin, D., Lan, X., Leuenberger, M., Lindauer, M., Lopez, M., Manca, G., Müller-Williams, J., O'Doherty, S., Scheeren, B., Steinbacher, M., Trisolino, P., Vítková, G., and Kwok, C. Y.: High-resolution inverse modelling of European CH<sub>4</sub> emissions using novel FLEXPART-COSMO TM5 4DVAR inverse modelling system, *Atmospheric Chem Phys Discuss*, 2022, 1–37, <https://doi.org/10.5194/acp-2022-118>, 2022.

Buitenhuis, E. T., Suntharalingam, P., and Quéré, C. L.: Constraints on global oceanic emissions of N<sub>2</sub>O from observations and models, *Biogeosciences*, 15, 2161–2175, <https://doi.org/10.5194/bg-15-2161-2018>, 2018.

Etiopie, G., Ciotoli, G., Schwietzke, S., and Schoell, M.: Gridded maps of geological methane emissions and their isotopic signature, *Earth Sys Sci Data*, 11, 1–22, <https://doi.org/10.5194/essd-11-1-2019>, 2019.

Fortems-Cheiney, A., Pison, I., Broquet, G., Dufour, G., Berchet, A., Potier, E., Coman, A., Siour, G., and Costantino, L.: Variational regional inverse modeling of reactive species emissions with PYVAR-CHIMERE-v2019, *Geosci Model Dev*, 14, 2939–2957, <https://doi.org/10.5194/gmd-14-2939-2021>, 2021.

Jackson, R. B., Saunois, M., Bousquet, P., Canadell, J. G., Poulter, B., Stavert, A. R., Bergamaschi, P., Niwa, Y., Segers, A., and Tsuruta, A.: Increasing anthropogenic methane emissions arise equally from agricultural and fossil fuel sources, *Environ Res Lett*, 15, 1–8, <https://doi.org/10.1088/1748-9326/ab9ed2>, 2020.

Reza Koohkan, M., & Bocquet, M. Accounting for representativeness errors in the inversion of atmospheric constituent emissions: application to the retrieval of regional carbon monoxide fluxes. *Tellus B: Chemical and Physical Meteorology*, 64(1), 19047, 2012.

Petrenko, V. V., Smith, A. M., Schaefer, H., Riedel, K., Brook, E., Baggenstos, D., Harth, C., Hua, Q., Buizert, C., Schilt, A., Fain, X., Mitchell, L., Bauska, T., Orsi, A., Weiss, R. F., and Severinghaus, J. P.:

Minimal geological methane emissions during the Younger Dryas–Preboreal abrupt warming event, *Nature*, 548, 443–446, <https://doi.org/10.1038/nature23316>, 2017.

Pisso, I., Sollum, E., Grythe, H., Kristiansen, N., Cassiani, M., Eckhardt, S., Arnold, D., Morton, D., Thompson, R. L., Zwaaftink, C. D. G., Evangeliou, N., Sodemann, H., Haimberger, L., Henne, S., Brunner, D., Burkhart, J. F., Fouilloux, A., Brioude, J., Philipp, A., Seibert, P., and Stohl, A.: The Lagrangian particle dispersion model FLEXPART version 10.3, *Geosci Model Dev*, 2019, 1–67, <https://doi.org/10.5194/gmd-2018-333>, 2019.

Saunois, M., Stavert, A. R., Poulter, B., Bousquet, P., Canadell, J. G., Jackson, R. B., Raymond, P. A., Dlugokencky, E. J., Houweling, S., Patra, P. K., Ciais, P., Arora, V. K., Bastviken, D., Bergamaschi, P., Blake, D. R., Brailsford, G., Bruhwiler, L., Carlson, K. M., Carrol, M., Castaldi, S., Chandra, N., Crevoisier, C., Crill, P. M., Covey, K., Curry, C. L., Etiope, G., Frankenberg, C., Gedney, N., Hegglin, M. I., Iqbal, K., Ishizawa, M., Ito, A., Janssens-Maenhout, G., Jensen, K. M., Joos, F., Kleinen, T., Krummel, P. B., Langenfelds, R. L., Laruelle, G. G., Liu, L., Machida, T., Maksyutov, S., McDonald, K. C., McNorton, J., Miller, P. A., Melton, J. R., Morino, I., Müller, J. M., Murgia-Flores, F., Naik, V., Niwa, Y., Noce, S., O’Doherty, S., Parker, R. J., Peng, C., Peng, S., Peters, G. P., Prigent, C., Prinn, R., Ramonet, M., Regnier, P., Riley, W. J., Rosentreter, J. A., Segers, A., Simpson, I. J., Shi, H., Smith, S. J., Steele, P. L., Thornton, B. F., Tian, H., Tohjima, Y., Tubiello, F. N., Tsuruta, A., Viovy, N., Voulgarakis, A., Weber, T. S., Weele, M. van, Werf, G. R. V. der, Weiss, R. F., Worthy, D., Wunch, D., Yin, Y., Yoshida, Y., Zhang, W., Zhang, Z., Zhao, Y., Zheng, B., Zhu, Q., and Zhuang, Q.: The Global Methane Budget 2000–2017, *Earth Sys Sci Data*, 12, 1561–1623, <https://doi.org/10.5194/essd-12-1561-2020>, 2020.

Seibert, P. and Frank, A.: Source-receptor matrix calculation with a Lagrangian particle dispersion model in backward mode, *Atmos Chem Phys*, 4, 51–63, <https://doi.org/10.5194/acp-4-51-2004>, 2004.

Stohl, A., Forster, C., Frank, A., Seibert, P., and Wotawa, G.: Technical note: The Lagrangian particle dispersion model FLEXPART version 6.2, *Atmos. Chem. Phys.*, 5, 2461–2474, <https://doi.org/10.5194/acp-5-2461-2005>, 2005.

Szénási, B., Berchet, A., Broquet, G., Segers, A., Gon, H. D. van der, Krol, M., Hulleger, J. J. S., Kiesow, A., Günther, D., Petrescu, A. M. R., Saunois, M., Bousquet, P., and Pison, I.: A pragmatic protocol for characterising errors in atmospheric inversions of methane emissions over Europe, *Tellus B Chem Phys Meteorology*, 73, 1–23, <https://doi.org/10.1080/16000889.2021.1914989>, 2021.

Thompson, R. L. and Stohl, A.: FLEXINVERT: an atmospheric Bayesian inversion framework for determining surface fluxes of trace species using an optimized grid, *Geosci Model Dev*, 7, 2223–2242, <https://doi.org/10.5194/gmd-7-2223-2014>, 2014.

Zaehle, S., Ciais, P., Friend, A. D., and Prieur, V.: Carbon benefits of anthropogenic reactive nitrogen offset by nitrous oxide emissions, *Nature*, 4, 601–605, 2011.

Zwaaftink, C. D. G., Henne, S., Thompson, R. L., Dlugokencky, E. J., Machida, T., Paris, J.-D., Sasakawa, M., Segers, A., Sweeney, C., and Stohl, A.: Three-dimensional methane distribution simulated with FLEXPART 8-CTM-1.1 constrained with observation data, *Geosci. Model Dev.*, 11, 4469–4487, <https://doi.org/10.5194/gmd-11-4469-2018>, 2018.